

Turbulence modulation in buoyancy-driven bubbly flows

Vikash Pandey¹, Dhrubaditya Mitra² and Prasad Perlekar¹

¹TIFR Centre for Interdisciplinary Sciences, Tata Institute of Fundamental Research, Gopanpally, Hyderabad 500046, India

²Nordita, KTH Royal Institute of Technology and Stockholm University, Roslagstullsbacken 23, 10691 Stockholm, Sweden

(Received xx; revised xx; accepted xx)

We present a Direct Numerical Simulation (DNS) study of buoyancy-driven bubbly flows in the presence of large scale driving that generates turbulence. On increasing the turbulence intensity: (a) the bubble trajectories become more curved, and (b) the average rise velocity of the bubbles decreases. We find that the energy spectrum of the flow shows a pseudo-turbulence scaling for length scales smaller than the bubble diameter and a Kolmogorov scaling for scales larger than the bubble diameter. We conduct a scale-by-scale energy budget analysis to understand the scaling behaviour observed in the spectrum. Although our bubbles are weakly buoyant, the statistical properties of our DNS are consistent with the experiments that investigate turbulence modulation by air bubbles in water.

Key words:

1. Introduction

The flow of suspension of deformable objects (bubbles or droplets) is omnipresent in a variety of natural and industrial processes (Mudde 2005; Balachandar & Eaton 2010; Risso 2018; Said 2019; Mathai *et al.* 2020). The presence of particles dramatically alters the rheological and thereby mixing properties of flows (Almeras *et al.* 2019; Alméras *et al.* 2015; Rosti *et al.* 2018; Rosti & Brandt 2018). A swarm of rising bubbles in an otherwise quiescent fluid, at moderate volume-fraction, generates pseudo-turbulence studied by several experiments and numerical simulations over the last three decades (Lance & Bataille 1991; Mudde 2005; Risso 2018; Mathai *et al.* 2020; Pandey *et al.* 2020).

A more complex but ubiquitous scenario is where large scale external stirring that generates turbulence is also present along with the bubbles (Deckwer 1992; Tabib *et al.* 2008; Mathai *et al.* 2020). In the absence of bubbles, a nonlinear

transfer of energy (maintaining constant energy flux) from forcing to dissipation range characterizes turbulence (Kolmogorov 1941; Frisch 1997; Pope 2012). How does the presence of bubbles modify this flow? The answer, in principle, depends on the ratio of the bubble diameter to the dissipation scale, the bubble volume fraction, and its density and viscosity contrast with the ambient fluid.

Experiments with large scale forcing that generates nearly homogeneous and isotropic flows, at large Reynolds number, show that the presence of bubbles dramatically alters the energy spectrum for scales smaller than the bubble diameter (Prakash *et al.* 2016; Almeras *et al.* 2017). Although the liquid velocity fluctuations have been well-characterized, an understanding of the energy transfer mechanisms remain mostly unexplored.

Direct Numerical Simulation (DNS) studies of bubbly flows have explored: a) buoyancy-driven flows that generate pseudo-turbulence or bubble induced agitation in the absence of external stirring (Bunner & Tryggvason 2002*b,a*; Roghair *et al.* 2011; Pandey *et al.* 2020; Ramadugu *et al.* 2020; Innocenti *et al.* 2021), b) modulation of turbulence by suspension of neutrally buoyant particles (Rosti *et al.* 2019; Yousefi *et al.* 2020), and c) Lagrangian investigations of an isolated bubble in the presence of external stirring (Loisy & Naso 2017). However, to the best of our knowledge, a numerical study designed to unravel the statistical properties of buoyancy-driven bubbly flows in presence of external stirring is still missing.

Most numerical studies are restricted to low or moderate Galilei numbers because extremely fine grids are required to fully resolve bubbles with high-density and viscosity contrasts (for e.g., air bubbles in water) (Cano-Lozano *et al.* 2016; Innocenti *et al.* 2021). Furthermore, the use of second-order finite-difference methods limits the range of Reynolds numbers accessible to these simulations (Canuto *et al.* 2012).

Fortunately, the DNS studies of buoyancy-driven bubbly flow have shown that the statistical properties of pseudo-turbulence such as the PDF of velocity fluctuations, the scaling of the energy spectrum, and the energy transfer mechanisms are universal and do not depend upon density and viscosity ratios (Pandey *et al.* 2020; Ramadugu *et al.* 2020; Innocenti *et al.* 2021). A key finding of these studies is the presence of energy flux from length scales corresponding to the bubble diameter to small scales. This has also been confirmed in a recent study on bubble-laden turbulent channel flow (Ma *et al.* 2021). Motivated by these findings, in this article, we investigate turbulence modulation in suspensions of weakly buoyant bubbles. Similar to the experiments, we characterize the flow in terms of the ‘bubblance’ parameter $b = \Phi (V_0/u_0)^2$, where Φ is the bubble volume fraction, V_0 is the rise velocity of an isolated bubble in a quiescent fluid, and u_0 is the r.m.s. velocity of the turbulent flow in the absence of bubbles. The two extreme limits $b = 0$ and $b = \infty$ correspond to pure fluid turbulence and buoyancy-driven bubbly flow, respectively.

2. Model

We simulate the Navier-Stokes (NS) equations with a surface tension force to investigate the suspension of bubbles. Since we are interested in studying the weakly buoyant regime, we invoke the Boussinesq approximation (Chandrasekhar

1981; Pandey *et al.* 2020) to get,

$$D_t \mathbf{u} = \nu \nabla^2 \mathbf{u} - \nabla P + \mathbf{F}^\sigma + \mathbf{F}^g + \mathbf{F}^s, \text{ and } \nabla \cdot \mathbf{u} = 0. \quad (2.1)$$

Here \mathbf{u} is the velocity field, $D_t \equiv \partial_t + \mathbf{u} \cdot \nabla$ is the material derivative, P is the pressure field, and ν is the viscosity (assumed to be identical in the two phases). The two phases are distinguished using an indicator function c which is equal to 1 in the liquid and 0 inside bubble (Popinet 2018; Tryggvason *et al.* 2001). The buoyancy force $\mathbf{F}^g \equiv 2At[c - c_a]\mathbf{g}$, where c_a is the mean value of the indicator function, $At \equiv (\rho_f - \rho_b)/(\rho_f + \rho_b)$ is the Atwood number, $\mathbf{g} \equiv -g\hat{\mathbf{z}}$ is the acceleration due to gravity, $\hat{\mathbf{z}}$ is a unit vector along the vertical (positive z) direction, and ρ_f (ρ_b) is the fluid (bubble) density. The surface tension force is $\mathbf{F}^\sigma \equiv \sigma\kappa\hat{\mathbf{n}}$, where κ is the local curvature of the bubble-front whose unit normal is $\hat{\mathbf{n}}$, and σ is the coefficient of the surface tension. Turbulence is generated using a large scale stirring force \mathbf{F}^s . For a detailed discussion on the Boussinesq approximation, we refer the reader to Appendix A. Experimentally small Atwood At (weakly buoyant regime) number flows can be realized in a mixture of oils (Shukla *et al.* 2019; Yi *et al.* 2021).

We use a pseudo-spectral method (Canuto *et al.* 2012) for the DNS of (2.1) in a periodic cube with each side of length $L \equiv 2\pi$. The bubbles are resolved using a front-tracking method. The same method had been earlier employed by us to investigate buoyancy-driven bubbly flows in absence of turbulent stirring (Pandey *et al.* 2020; Ramadugu *et al.* 2020). For a detailed discussion on the numerical implementation of front-tracking method to study a variety of multiphase flows, we refer the reader to Tryggvason *et al.* (2001); Popinet (2018).

For time-evolution, we use a second-order exponential time differencing scheme (Cox & Matthews 2002) for (2.1) and a second-order Runge-Kutta scheme to update the front. A substantial part of the computational effort is spent in resolving the front; DNS with the bubbles is four times slower than the one without them. The large-scale stirring force is implemented in Fourier space, i.e., $\hat{\mathbf{F}}^s = \varepsilon^s \hat{\mathbf{u}} / \sum_{\mathbf{k}} |\hat{\mathbf{u}}|^2$ with $|\mathbf{k}| \leq k_{\text{inj}}$ (Machiels 1997; Petersen & Livescu 2010; Perlekar 2019), where $\hat{\mathbf{u}}$ is the Fourier transform of \mathbf{u} and $k_{\text{inj}} = 2$. This implementation ensures a constant rate of energy injection, ε^s .

We discretize the simulation domain with N^3 collocation points, set the initial velocity field such that the corresponding energy spectrum $E(k, t = 0) = \varepsilon^s k^4 \exp(-4k^2)$, and place $N_b = 80$ non-overlapping spherical bubbles of diameter $d = 0.46$ at random locations such that no two bubbles overlap.

The dimensionless numbers that characterize the flow are the Taylor-scale Reynolds number $\text{Re}_\lambda \equiv u_0 \lambda / \nu$, the Galilei number $\text{Ga} \equiv \sqrt{2Atgd^3/\nu^2}$ the Bond number $\text{Bo} \equiv 2At\rho_a g d^2 / \sigma$, and the bubble parameter $b \equiv \Phi (V_0/u_0)^2$, where $\Phi \equiv N_b(\pi/6)(d/L)^3$ is the volume fraction occupied by the bubbles, $V_0 \approx 0.8$ is the rise speed of a single bubble of diameter d in quiescent fluid, $\lambda \equiv \sqrt{15\nu u_0^2/\varepsilon^s}$ is the Taylor-microscale, $u_0 \equiv \sqrt{2E/3}$ is the r.m.s. velocity in absence of bubbles, $E \equiv \langle |\mathbf{u}|^2 \rangle / 2$ is the average kinetic energy, we set the average density $\rho_a = 1$. The parameters used in our DNS are summarized in table 1. We conduct a grid-resolution study in Appendix B to show that our simulations are well resolved.

runs	N	Re_λ	$\varepsilon^\nu \times 10^{-2}$	$\varepsilon^s \times 10^{-2}$	$\varepsilon^g \times 10^{-3}$	λ	$\eta \times 10^{-2}$	b
R0	720	–	0.7	–	7.0	–	–	∞
R1	720	79	0.9	0.25	6.8	0.37	2.0	0.35
R2	720	95	1.2	0.5	6.7	0.34	1.8	0.21
R3	720	110	1.5	1.0	6.0	0.31	1.5	0.13

Table 1: Parameters for our DNS runs R0 – 3. Here, $\varepsilon^\nu = \nu \langle |\nabla \mathbf{u}|^2 \rangle$ is the viscous dissipation rate, $\eta \equiv (\nu^3/\varepsilon^s)^{1/4}$ is the Kolmogorov dissipation scale, λ is the Taylor microscale, the energy injection rates due to large scale stirring and buoyancy are $\varepsilon^s \equiv \langle \mathbf{u} \cdot \mathbf{F}^s \rangle$ and $\varepsilon^g \equiv \langle \mathbf{u} \cdot \mathbf{F}^g \rangle$, respectively. The angular brackets denote spatio-temporal averaging in the statistically steady-state. For all the runs $L = 2\pi$, $d = 0.46$, and the dimensionless numbers $\text{Ga} = 302$, $\text{Bo} = 1.8$, $\text{At} = 0.04$, and $\Phi = 1.64\%$ are kept fixed. We run simulations R1 – R3 at least for a period of $\approx 5\tau_L$ in the steady-state, where $\tau_L \equiv L/(2u_0)$ is the large eddy turn over time. The simulation R0 runs for a period of $10L/V_0$ in the steady-state. The values of Φ , Ga , Bo , and Re_λ used in our study are comparable to those used in the experiments (Prakash *et al.* 2016; Almeras *et al.* 2017).

3. Results

In what follows, we first investigate the statistical properties of bubbles rising in the turbulent flow, we then investigate the statistical properties of the fluid velocity fluctuations. Although we study turbulence modulation in the presence of weakly buoyant bubbles, we show in the subsequent sections that the statistical properties of the flow are in qualitative agreement with experiments that typically have large density and viscosity contrast. Finally, we present the results for the spectral properties of the flow by using a scale-by-scale energy budget analysis.

3.1. Bubble trajectories and rise velocity

For every bubble, we monitor the time evolution of its center-of-mass $\mathbf{X}_i(t)$ after every $\delta t = 0.08\tau_\eta$ time interval, where i denotes the bubble index, and $\tau_\eta = \sqrt{\nu/\varepsilon^s}$ is the Kolmogorov dissipation time scale. From the bubble tracks, we obtain the center-of-mass velocity $\mathbf{V}_i(t)$ and the acceleration $\mathbf{A}_i(t)$ using centered, second-order, finite-differences.

The plots in figure (1a-b) show a representative snapshot of bubbles and iso-vorticity surfaces for $\text{Re}_\lambda = 79$, $b = 0.35$ and $\text{Re}_\lambda = 110$, $b = 0.13$, respectively. In figure (1c-d) we show a few typical trajectories for the same parameters. It is clear that higher Reynolds number and small ‘bubbance’ parameter corresponds to more complex trajectories. To quantify this behaviour we plot the probability distribution function (PDF) of the curvature $\mathcal{K} \equiv |\mathbf{A} \times \mathbf{V}| / |\mathbf{V}|^3$ in figure (1e). Consistent with the observation that the trajectories are more curved for larger Re_λ , we find that the probability distribution function $P(\mathcal{K})$ is broader– has an exponential tail.

Note that, Bhatnagar *et al.* (2016) showed that the PDF, of curvature of trajectories of heavy inertial particles in homogeneous and isotropic turbulence, has a power-law tail with an exponent of $-5/2$. To the best of our knowledge no such results exists for bubbles.

Another consequence of large-scale turbulent stirring is that the average bubble rise velocity $U \equiv (1/N_b) \sum_{i=1}^{N_b} \overline{\mathbf{V}_i(t) \cdot \hat{\mathbf{z}}}$ (see figure (1f)) increases with increasing b (decreasing Re_λ), where $\overline{(\cdot)}$ represents temporal averaging.

In a recent study, Salibindla *et al.* (2020) show that the rise velocity of the bub-

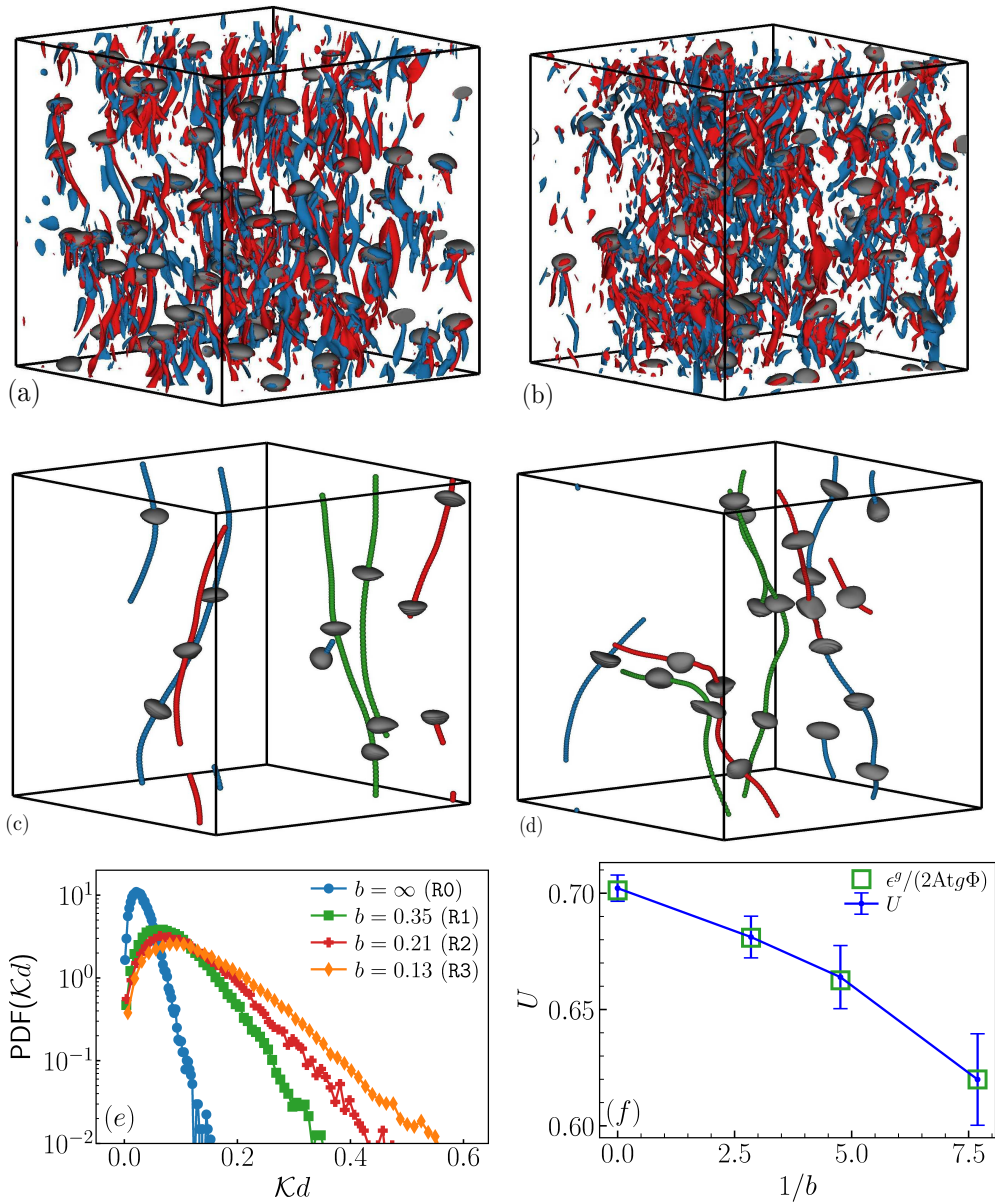


Figure 1: Top panel: Representative steady-state snapshot of the bubbles and super-imposed iso-surfaces of the z -component of the vorticity field $\omega_z = \hat{z} \cdot \nabla \times \mathbf{u}$ for $\omega_z = \pm 3 \langle \omega_z^2 \rangle^{1/2}$ for (a) $b = 0.35$, and (b) $b = 0.13$. Middle panel: Typical trajectories of the center-of-mass of bubbles in a turbulent flow for (c) $\text{Re}_\lambda = 79, b = 0.35$ (R1) and (d) $\text{Re}_\lambda = 110, b = 0.13$ (R3). Bottom panel: (e) The PDF of the curvature \mathcal{K} for different values of b . (f) Plot showing that the bubble rise velocity increases with increasing b or decreasing Re_λ . We also show that U obtained directly from the trajectories and the estimate $\varepsilon^{\mathcal{S}}/(2\text{At}g\Phi)$ are in excellent agreement.

runs	R1	R2	R3
γ	58.3	36.7	23.1

Table 2: Velocity ratio γ for our DNS runs R1 – 3

bles can be enhanced by turbulence provided the velocity ratio $\gamma \equiv (V_0^2/(\varepsilon^s d)^{2/3}) < 1$. Our DNS (see Table 2) and the experiments that investigate turbulence modulation by bubbles (Lance & Bataille 1991; Prakash *et al.* 2016) have $\gamma \gg 1$.

Note that even for $b = \infty$, the rise velocity of a bubble in a swarm is slightly smaller than the rise velocity of an isolated bubble due to bubble-wake interactions (Riboux *et al.* 2010). Using the definition of \mathbf{F}^g and noting that $\langle u_z \rangle = 0$ in the Boussinesq regime, we obtain $\varepsilon^g = 2Atg\Phi U$ and verify it in figure (1f).

3.2. Pair Distribution Function

To understand the distribution of bubbles in the domain, following Bunner & Tryggvason (2002a), we define the pair distribution function,

$$G[r, \cos(\theta)] = \frac{L^3}{N_b(N_b - 1)} \sum_{i=1}^{N_b} \sum_{j=1, j \neq i}^{N_b} \overline{\delta(\mathbf{r} - \mathbf{X}_{ij}, t)}, \quad (3.1)$$

where $\delta(\cdot)$ is the Dirac delta function, and $\mathbf{X}_{ij} = \mathbf{X}_i - \mathbf{X}_j$. In figure (2a), we sketch a bubble pair configuration to show the co-ordinate system used for evaluating (3.1). The plot of $G[r, \cos(\theta)]$ for $r = 2d$ and $4d$ is shown in figure (2b). At $b = \infty$, we observe a peak in $G[r, \cos(\theta)]$ for $r \approx 2d$ and $\cos(\theta) \approx 0$ indicating a horizontal alignment of bubbles that are separated by a distance $2d$. Bubbles separated by distances, $r \geq 4d$ are uniformly distributed. Our results are consistent with earlier numerical studies of pseudo-turbulence (Bunner & Tryggvason 2002a; Roghair *et al.* 2013). In contrast, as turbulence makes flow more isotropic, for $b = 0.13$ we find that $G[r, \cos(\theta)]$ is uniform which indicates that the bubbles are uniformly distributed for all separations r .

3.3. Average flow around a bubble

In this section, we study the average wake structure of the bubbles for different values of bubble b . At a given time t , the velocity field in the center-of-mass frame of the bubble i is given by

$$\mathbf{u}_i^{\text{CM}}(\boldsymbol{\xi}, t) = \mathbf{u}(\boldsymbol{\xi}, t) - \mathbf{V}_i, \quad (3.2)$$

where $\boldsymbol{\xi} \equiv \mathbf{x} - \mathbf{X}_i$ and $-L/2 < (\xi_x, \xi_y, \xi_z) \leq L/2$. The average flow around a bubble is then obtained by performing temporal averaging over every bubble as follows

$$\mathbf{u}^{\text{CM}}(\boldsymbol{\xi}) = \frac{1}{N_b} \sum_{i=1}^{N_b} \overline{\mathbf{u}_i^{\text{CM}}(\boldsymbol{\xi}, t)}. \quad (3.3)$$

In figure (3a,b) we plot the velocity streamlines of the average velocity field $\mathbf{u}^{\text{CM}}(\boldsymbol{\xi})$ for $b = \infty$ (R0) and $b = 0.13$ (R3). Although the flow structure look qualitatively similar, we find that the bubble in the absence of large scale stirring

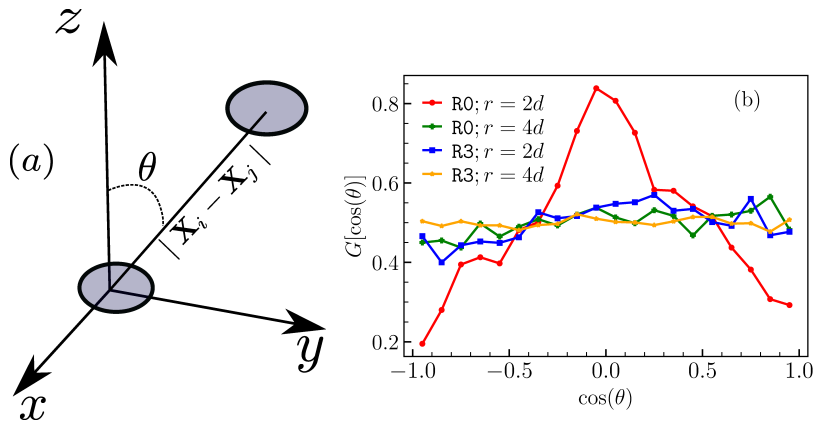


Figure 2: (a) The separation vector $\mathbf{r} = \mathbf{X}_i - \mathbf{X}_j$, and the angle θ between the \mathbf{X}_{ij} and $\hat{\mathbf{z}}$. The bubbles are represented as shaded ellipse. (b) The angular distribution function $G[r, \cos(\theta)]$ versus $\cos(\theta)$ for $r = 2d$, and $r = 4d$ in absence (presence) $b = \infty$ ($b = 0.13$) of turbulence. The area under the curve is normalized to unity for each $G[r, \cos(\theta)]$ curve.

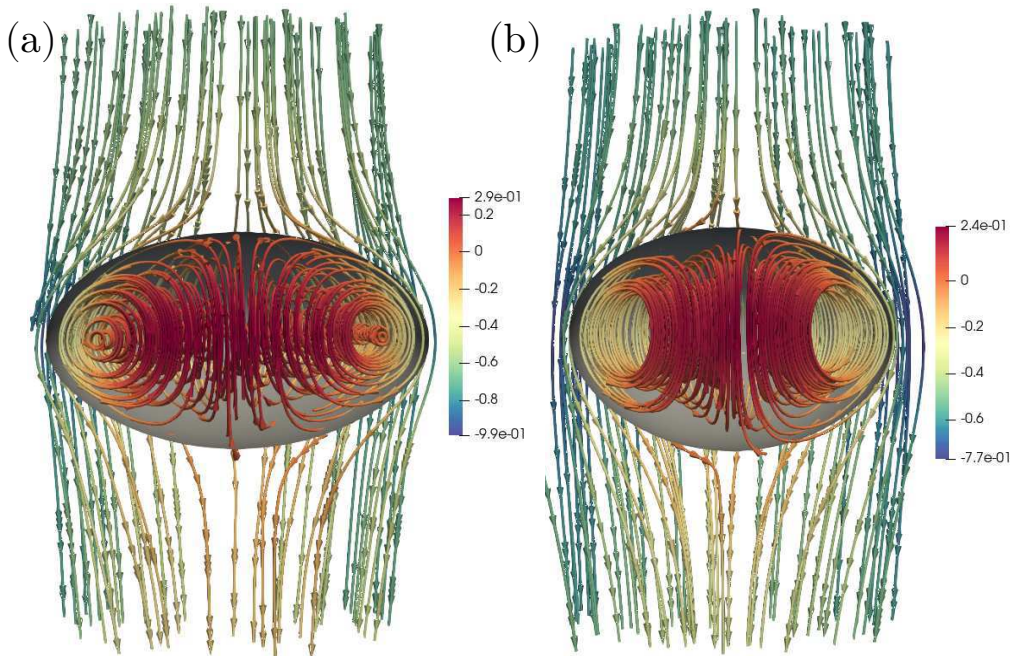


Figure 3: The streamline plot of the average velocity field in the frame of bubble for (a) $b = \infty$ run R0 and (b) $b = 0.13$ run R3. The streamlines are colored according to $\mathbf{u}^{\text{CM}} \cdot \hat{\mathbf{z}}$

is more ellipsoidal. This can be understood by noting that presence of stirring imposes stronger isotropy on the flow.

To quantify, the behavior of the average bubble wake, similar to the experiments (Risso *et al.* 2008; Almeras *et al.* 2017) we plot $v(\xi_z) \equiv \mathbf{u}^{\text{CM}}(0, 0, \xi_z) \cdot \hat{\mathbf{z}}$ in figure (4) and find that it decays exponentially $v(\xi_z) \sim C \exp(-A\xi_z/d)$ in the wake region for all values of b . However, consistent with earlier observations, presence of stirring leads to a faster decay of the wake. Therefore, for small b (or large Re_λ) we

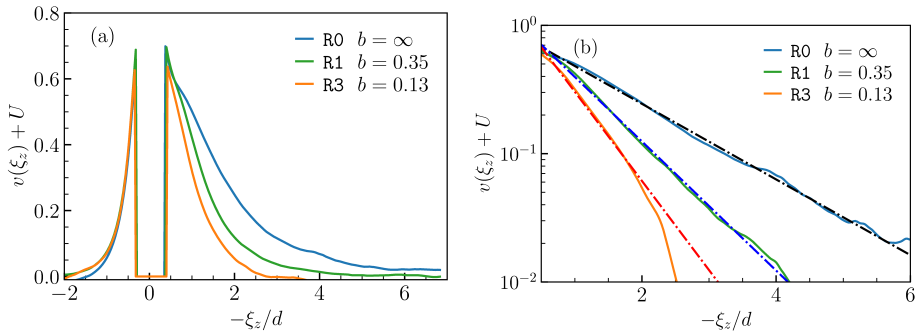


Figure 4: (a) The average bubble wake velocity $v(\xi_z)$ for run R0 ($b = \infty$), R1 ($b = 0.35$), and R3 ($b = 0.13$). (b) Same as (a), but in semi-log scale to highlight the exponential decay of the velocity field in the wake region. The dashed-dot line show the exponential fits $\sim \exp(-Az/d)$ to the data. We find $A = 0.67, 1.15$ and 1.6 for R0, R1, and R3 respectively.

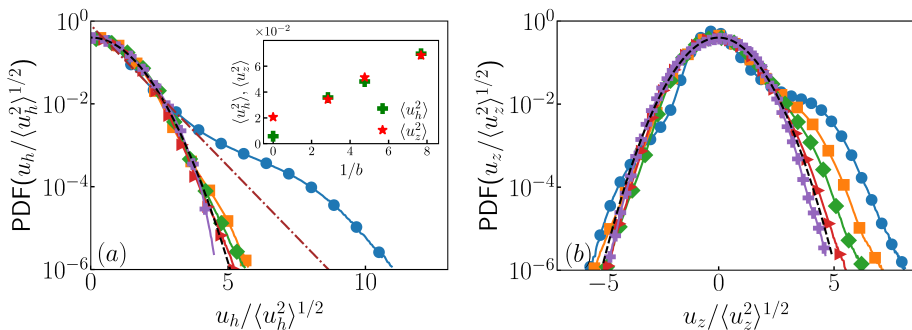


Figure 5: The PDF of the horizontal (a) and the vertical (b) component of the liquid velocity fluctuations for different values of b [\bullet $b = \infty$ (R0), \blacksquare $b = 0.35$ (R1), \blacklozenge $b = 0.21$ (R2), \blacktriangleright $b = 0.13$ (R3), \blacktriangleleft $b = 0$ ($\text{Re}_\lambda = 110$)]. The black dashed line indicates a Gaussian distribution, and the brown dash-dot line in panel (a) shows the exponential distribution. (Inset) Variance of the horizontal and vertical velocity fluctuations increases with an increase in the stirring intensity $1/b$.

expect (see next section) the velocity fluctuations to be similar to homogeneous, isotropic turbulence.

3.4. Liquid velocity fluctuations

The PDFs of the normalized horizontal and vertical liquid velocity fluctuation with varying b are shown in figure (5). For $b = \infty$, our results agree with the earlier studies on pseudo-turbulence (Riboux *et al.* 2010; Risso 2016; Pandey *et al.* 2020): the PDF of the horizontal component shows exponential behaviour and the PDF of the vertical component has a Gaussian core and is positively skewed. The presence of external stirring dramatically alters the PDFs as they tend to a Gaussian distribution with decreasing b (increasing Re_λ). Indeed, in figure (5a,inset) we verify that $\langle u_h^2 \rangle \sim \langle u_z^2 \rangle$ on decreasing b confirming that the stirring makes the flow isotropic. This is consistent with earlier experimental observations on turbulent bubbly flows (Prakash *et al.* 2016; Almeras *et al.* 2017).

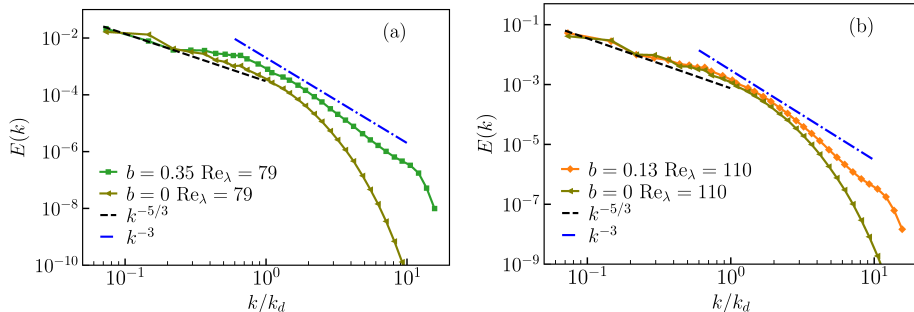


Figure 6: Log-log plot of the kinetic energy spectrum, $E(k)$ versus k/k_d for (a) $b = 0.35$, $\text{Re}_\lambda = 79$ (R1) and (b) $b = 0.13$, $\text{Re}_\lambda = 110$ (R3).

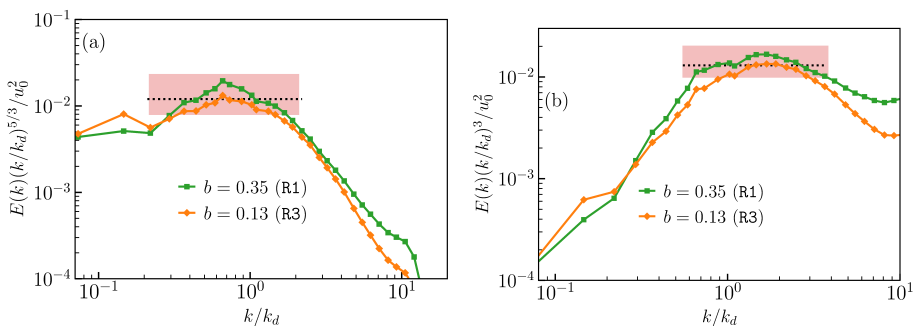


Figure 7: Compensated plot of the kinetic energy spectrum highlighting the (a) $-5/3$, and (b) -3 scaling ranges. Horizontal dashed line and the shaded region indicate the scaling range.

3.5. Energy spectrum

Earlier DNS studies (Roghair *et al.* 2011; Pandey *et al.* 2020; Innocenti *et al.* 2021) have only investigated the nature of the energy spectrum in the absence of large scale turbulent forcing. These studies, consistent with experiments, confirm the presence of a k^{-3} scaling in the spectrum that appears because of the balance of net energy production in the wakes with viscous dissipation.

Experiments have investigated temporal spectrum of the Eulerian liquid velocity fluctuations in presence of a large scale stirring. They observe a Kolmogorov spectrum for frequencies smaller than the bubble frequency and a pseudo-turbulence scaling for higher frequencies (Lance & Bataille 1991; Prakash *et al.* 2016; Almeras *et al.* 2017).

Hence we expect that in our simulations we would find a Kolmogorov scaling, for wavenumbers $k < k_d$, with a crossover to pseudo-turbulence scaling for $k > k_d$, where $k_d \equiv 2\pi/d$ is the wavenumber corresponding to the bubble diameter.

In figure (6), we plot the scaled energy spectrum for different values of b (Re_λ). As expected, we observe Kolmogorov scaling $E(k) \sim k^{-5/3}$ for $k < k_d$ and a pseudo-turbulence scaling $E(k) \sim k^{-3}$ for $k > k_d$. In figure (7a,b) we plot the compensated spectrum to highlight the region showing $-5/3$ and -3 scaling. Note that none of the scaling ranges are large enough to make an accurate determination of the scaling exponent possible.

3.6. Scale-by-scale energy budget and flux

To lay bare the mechanism by which bubbly turbulence emerge we study the scale-by-scale energy budget. Following Pope (2012) we define a low-pass filtered velocity field coarse-grained at scale $\ell = 2\pi/K$ as

$$\mathbf{u}_K^<(\mathbf{x}) \equiv \int \exp(i\mathbf{q} \cdot \mathbf{x}) G_K(\mathbf{q}) \hat{\mathbf{u}}(\mathbf{q}) d\mathbf{q}, \text{ with } G_K(\mathbf{q}) \equiv \exp\left(-\frac{\pi^2 \mathbf{q}^2}{24K^2}\right). \quad (3.4)$$

Note that Frisch (1997); Pandey *et al.* (2020) use a sharp stepdown function as a filter: $G_K(\mathbf{q}) = 1$ for $|\mathbf{q}| \leq K$ and zero otherwise, whereas we use a smooth Gaussian filter (Pope 2012). In what follows, we use the symbol $(\cdot)_K^<$ to denote the filtering operation (Frisch 1997). In real space, this corresponds to

$$\mathbf{u}_K^<(\mathbf{x}) = \int G_\ell(\mathbf{r}) \mathbf{u}(\mathbf{x} - \mathbf{r}) d\mathbf{r}, \text{ with } G_\ell(\mathbf{r}) = \left(\frac{6}{\pi\ell^2}\right)^{\frac{1}{2}} \exp\left(-\frac{6r^2}{\ell^2}\right) \text{ and } \ell \equiv 2\pi/K.$$

Using the filtered velocity field, we obtain the following scale-by-scale energy budget equation from (2.1)

$$\Pi_K + \mathcal{F}_K^\sigma = -\mathcal{D}_K + \mathcal{F}_K^g + \mathcal{F}_K^s. \quad (3.5)$$

Here $\mathcal{F}_K^\sigma \equiv \langle \mathbf{u}_K^< \cdot (\mathbf{F}^\sigma)_K^< \rangle$ is the contribution from surface-tension forces, $\mathcal{F}_K^g \equiv \langle \mathbf{u}_K^< \cdot (\mathbf{F}^g)_K^< \rangle$ is the contribution from buoyancy, and $\mathcal{F}_K^s \equiv \langle \mathbf{u}_K^< \cdot (\mathbf{F}^s)_K^< \rangle$ is the contribution due to large-scale forcing. To obtain the contribution from the nonlinear term and viscous dissipation, following Eyink (1995); Borue & Orszag (1998); Pope (2012), we define a filtered version of the Reynolds stress tensor,

$$\mathbf{T}_K^{\alpha\beta}(\mathbf{x}) \equiv \left(u^\alpha u^\beta\right)_K^< - (u^\alpha)_K^< \left(u^\beta\right)_K^<, \quad (3.6)$$

the rate-of-strain tensor

$$\mathbf{S}_K^{\alpha\beta}(\mathbf{x}) \equiv \frac{1}{2} \left[\left(\partial_\alpha u^\beta\right)_K^< + \left(\partial_\beta u^\alpha\right)_K^< \right], \quad (3.7)$$

and the local nonlinear energy flux

$$\pi_K(\mathbf{x}) \equiv -\mathbf{T}_K^{\alpha\beta} \mathbf{S}_K^{\alpha\beta}. \quad (3.8)$$

Using (3.4), (3.6), (3.7), and (3.8), we get the net nonlinear flux $\Pi_K \equiv \langle \pi_K \rangle$, and the viscous contribution to the budget $\mathcal{D}_K \equiv 2\nu \langle \mathbf{S}_K^{\alpha\beta} \mathbf{S}_K^{\alpha\beta} \rangle$ which is always positive.

3.6.1. Scale-by-scale energy budget in the absence of bubbles: $b = 0$

In this case buoyancy makes no contribution to the fluxes and (3.5) simplifies to

$$\Pi_K = -\mathcal{D}_K + \mathcal{F}_K^s. \quad (3.9)$$

The plot in figure (8a) shows the energy budget for $b = 0$ ($\text{Re}_\lambda = 110$). Since the stirring force is limited to small Fourier modes $k \leq k_{\text{inj}}$, $\mathcal{F}_K^s = \mathcal{E}^s$ is a constant for $K > k_{\text{inj}}$. The viscous contribution \mathcal{D}_K is significant only for very large $K \geq k_\eta$. Hence, for intermediate values of K in the inertial range ($k_{\text{inj}} < K < k_\eta$), the flux $\Pi_K = \mathcal{F}_K^s$ remains a constant. The four-fifth law of Kolmogorov and the Kolmogorov scaling, $E(k) \sim k^{-5/3}$, is a consequence of this constancy of flux (see, e.g., Frisch 1997, section 6.2). Because of the moderate $\text{Re}_\lambda = 110$ used by

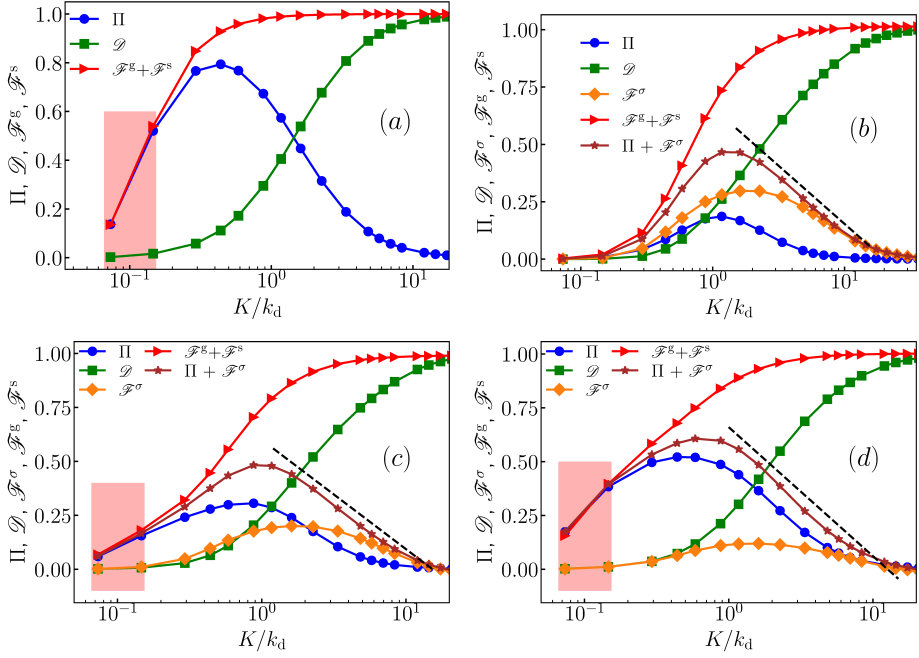


Figure 8: Scale-by-scale energy budget: plot of the energy flux Π_K , cumulative viscous dissipation \mathcal{D}_K , the surface tension contribution \mathcal{F}_K^σ , the cumulative energy injected due to buoyancy \mathcal{F}_K^b , and the energy injected due to turbulent forcing \mathcal{F}_K^s for $b = 0$ ($\text{Re}_\lambda = 110$) (a), $b = \infty$ (b), $b = 0.35$ (c), and $b = 0.13$ (d). The black dashed line indicates $\log(K)$ scaling. In (a-d) we normalize the ordinate by the viscous dissipation ε^ν . In panel (a), (c) and (d) we mark the injection wavenumbers by a shaded region.

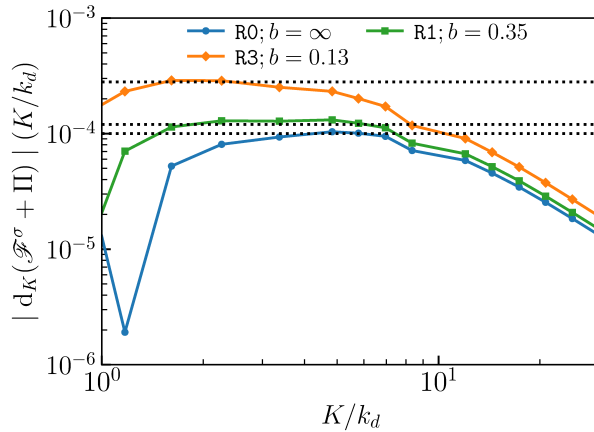


Figure 9: Log-log plot of $(K/k_d)|d(\mathcal{F}_K^\sigma + \Pi_K)/dK|$ versus K/k_d for different values of the bubble parameter b . Horizontal dashed lines represent K^{-1} scaling.

us, the range of wavenumbers over which the flux is constant is very small. A significant range of constant flux is observed in very high Re_λ and large resolution DNS (Ishihara *et al.* 2009).

3.6.2. Scale-by-scale budget in the absence of stirring ($b = \infty$):

Next, in figure (8b) we study the other extreme, $b = \infty$. Stirring makes no contribution here. Energy injection by buoyancy forces happens around the scale of the bubble diameters, the flux due to buoyancy \mathcal{F}_K^g becomes almost a constant for $K \gg k_d$. Hence for $K \gg k_d$ we obtain

$$\Pi_K + \mathcal{F}_K^\sigma = -\mathcal{D}_K + \mathcal{F}_K^g, \quad (3.10)$$

with \mathcal{F}_K^g approximately a constant. By taking a derivative of both sides of (3.10) with respect to K at $K = k$ we obtain

$$\left. \frac{d(\Pi_K + \mathcal{F}_K^\sigma)}{dK} \right|_{K=k} = \nu k^2 E(k). \quad (3.11)$$

Our DNS shows that the net production $\Pi_K + \mathcal{F}_K^\sigma \sim \log(K)$ (Lance & Bataille 1991; Pandey *et al.* 2020). Although, taking derivative can enhance approximation errors, we directly confirm the scaling relation in figure (9). Generalizing Lance & Bataille (1991) argument if we now assume locality of net transfer then by dimensional analysis $d(\Pi_K + \mathcal{F}_K^\sigma)/dK|_{K=k} \sim k^{-1}$ follows. Substituting in (3.11) we obtain $E(k) \sim k^{-3}$ – the spectrum of pseudo-turbulence (Lance & Bataille 1991; Mercado *et al.* 2010; Prakash *et al.* 2016; Almeras *et al.* 2017; Bunner & Tryggvason 2002b; Roghair *et al.* 2011; Pandey *et al.* 2020; Ramadugu *et al.* 2020). Risso (2011) has shown that the same k^{-3} -spectrum can be obtained, under certain conditions, as a sum of localized random, statistically independent, bursts; which comes from localized velocity disturbances caused by the bubbles.

3.6.3. Scale-by-scale budget in the presence of both bubbles and stirring

In figure (8c,d) we plot the energy budget for the two intermediate cases with $b = 0.35$ and $b = 0.13$. For $K \ll k_d$ both the buoyancy force and the surface tension contribute very little to the flux. The viscous contribution is also very small as $k_d < k_\eta$, the dissipation wavenumber. Let us also assume that there is a scale separation between the stirring scale, k_{inj} and k_d , with $k_{\text{inj}} \ll k_d$. Then for range of scales $k_{\text{inj}} < K < k_d$ the flux balance gives $\Pi_K = \mathcal{F}_K^s$, equal to a constant. Consequently we obtain $E(k) \sim k^{-5/3}$ for $k_{\text{inj}} < k < k_d$. Next we consider $K \gg k_d$: the net contribution from both stirring and buoyancy forces $\mathcal{F}_K^s + \mathcal{F}_K^g$ is almost a constant, hence we again obtain (3.11). Our DNS show that for both the bubble, $b = 0.35$, and 0.13 , $\Pi_K + \mathcal{F}_K^\sigma \sim \log(K)$ (see figure (9)). Although their individual contribution to the energy budget does depend on b , in particular: for $b = 0.13$, Π_K is larger than \mathcal{F}_K^σ , but for $b = 0.35$, Π_K is smaller than \mathcal{F}_K^σ . Hence for both of these cases we obtain $E(k) \sim k^{-3}$ for $k > k_d$ and $E(k) \sim k^{-5/3}$ for $k < k_d$.

In Appendix C, we show that qualitatively similar results are obtained even by using a sharp filter instead of a Gaussian filter.

3.6.4. Spatial distribution of the nonlinear energy flux $\pi_K(x)$

For homogeneous and isotropic turbulence, for any K in the inertial range, the net nonlinear flux Π_K is positive, i.e., on average energy flows from small to large K or from large to small spatial scales. Kraichnan (Kraichnan 1974; Eyink 1995) argued that the local nonlinear energy flux π_K (3.8) satisfies the refined similarity hypothesis. Using DNS, Chen *et al.* (2003) verified this and showed that

the scaling exponents of the flux show multiscaling. The multiscale analysis of the flux is also crucial to model subgrid scale dissipation in large-eddy simulations (Meneveau & Katz 2000).

To the best of our knowledge, the spatial distribution of local energy flux in bubbly flows remains unexplored. How does the sign of this flux correlate with the bubbles? For example, is the flux pre-dominantly positive in the wake of a bubble? In the following discussion, we address this question by performing a multiscale analysis of the local nonlinear energy flux $\pi_K(\mathbf{x})$ with varying filtering scale $\ell \sim 1/K$.

In figure (10), we show a typical snapshot from the run with no external stirring, $b = \infty$. The position of the bubbles is shown by plotting the indicator function in the top panel. In the middle and bottom panel, we plot the local nonlinear flux π_K . In each panel, we use four different values for the filtering wavenumber $K/k_d = 0.6, 1.0, 1.4$, and 2.2 , from left to right. Note that we use a Gaussian filter; therefore, a proper distinction between liquid and bubble phase can be made only for $K > k_d$. We make the following observations:

(i) In the front of the bubble, the energy is primarily transferred downscale, i.e., to scales smaller than $\ell \sim 1/K$.

(ii) Depending on the filtering scale, we observe both upscale and downscale transfer of energy in the wake of the bubble. For large K (small ℓ), downscale transfer of energy dominates the wake region, but there are also regions of upscale transfer.

(iii) On reducing the filter wavenumber K (large ℓ), we observe that the region of upscale transfer are enhanced in the aft region of the bubble. For the smallest filtering wavenumber $K/k_d = 0.6$, the front-aft region of the bubble has a similar structure but appears with opposite signs.

We can understand the fore-aft structure of the energy flux in the vicinity of a bubble in a straightforward manner. Consider a Stokesian spherical bubble with the same viscosity as ambient fluid rising in a quiescent flow; the stream function is given by the Hadamard-Rybczynski solution (Hadamard 1911; Rybczynski 1911; Clift *et al.* 1978):

$$\Psi(r, \theta) = \frac{V_0 r^2 \sin^2(\theta)}{2} \begin{cases} -\left(1 - \frac{5d}{8r} + \frac{d^3}{32r^3}\right), & \text{for } r \geq d/2, \\ \frac{1}{4}\left(1 - \frac{4r^2}{d^2}\right) & \text{for } r < d/2. \end{cases} \quad (3.12)$$

The radial and the angular component of the velocity field are $u_r = \partial_\theta \Psi / r^2 \sin(\theta)$ and $u_\theta = -\partial_r \Psi / r \sin(\theta)$. Using (3.12), we calculate the nonlinear flux π_K and plot it in figure (11) for four different values of the filtering wavenumber $K/k_d = 0.6, 1.0, 1.4$, and 2.2 . There is a downscale energy transfer in the front and a upscale energy transfer at the back side of the bubble. Note that the net energy flux Π_K is zero for the Hadamard-Rybczynski solution. Comparing figure (10) with figure (11), it seems that the spatial distribution of the energy flux comprises of a Hadamard-Rybczynski-like solution superimposed with turbulent fluctuations generated in the wake region of a rising bubble. Thus our multiscale analysis of the spatial energy flux provides a direct evidence that the net forward energy flux in figure (8b) is due to the bubble wakes.

The situation is more complex in presence of stirring, as now both the large scale forcing as well as the wake of the bubble creates complex spatio-temporal pattern

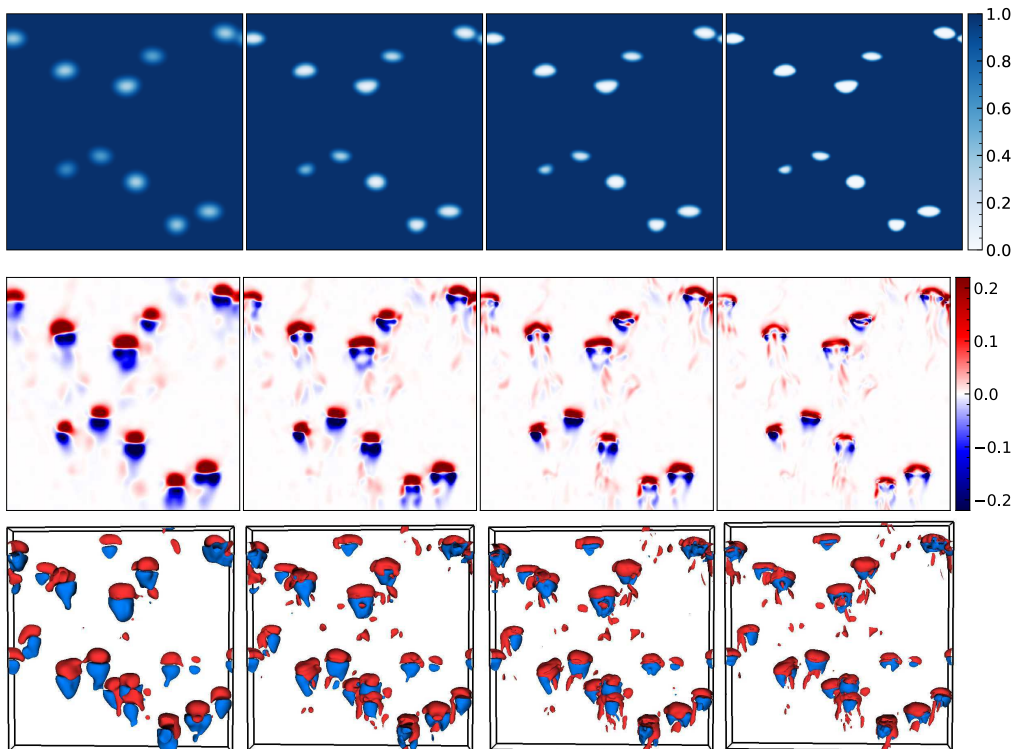


Figure 10: Buoyancy driven flow in absence of stirring ($b = \infty, R0$). The pseudocolor plot of the filtered indicator function c (top panel) and the local nonlinear flux $\pi_K / \max(\pi_{k_d})$ (middle panel) in the $y = L/2$ plane. Constant- π_K isosurfaces for $|\pi_K| = 0.03 \max(\pi_{k_d})$ in a slab $L \times 2d \times L$ around the $y = L/2$ plane (bottom panel). The filter wavenumber (scale) is increased (decreased) from left to right $K/k_d = 0.6, 1.0, 1.4$ and 2.2 .

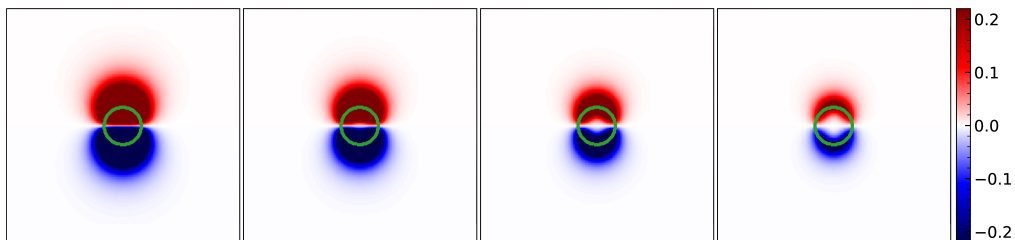


Figure 11: The space-dependent nonlinear flux $\pi_K / \max(\pi_{k_d})$ in the $y = L/2$ plane for the Hadamard-Rybczynski flow Eq. (3.12). The filter wavenumber (scale) is increased (decreased) from left to right $K/k_d = 0.6, 1.0, 1.4$ and 2.2 . The green line represents the bubble interface.

for $\pi_K(\mathbf{x})$ with regions of downscale and upscale transfer (see figure (12)). In figure (13) we plot the PDF of $\pi_K(\mathbf{x})$ with $K = k_d$ for $b = 0, 0.13$, and $b = \infty$. For all the cases we observe that the PDF is positively skewed confirming a net positive flux of energy. The skewness of the PDF for $b = 0$ is nearly 1.3 times larger than the $b = \infty$, indicating presence of stronger inverse energy transfers in buoyancy driven bubbly flows in comparison to homogeneous, isotropic turbulence. This is further verified by noting that the skewness for $b = 0.13$, where both stirring and buoyancy driven bubbles generate turbulence, is smaller than the case with $b = 0$.

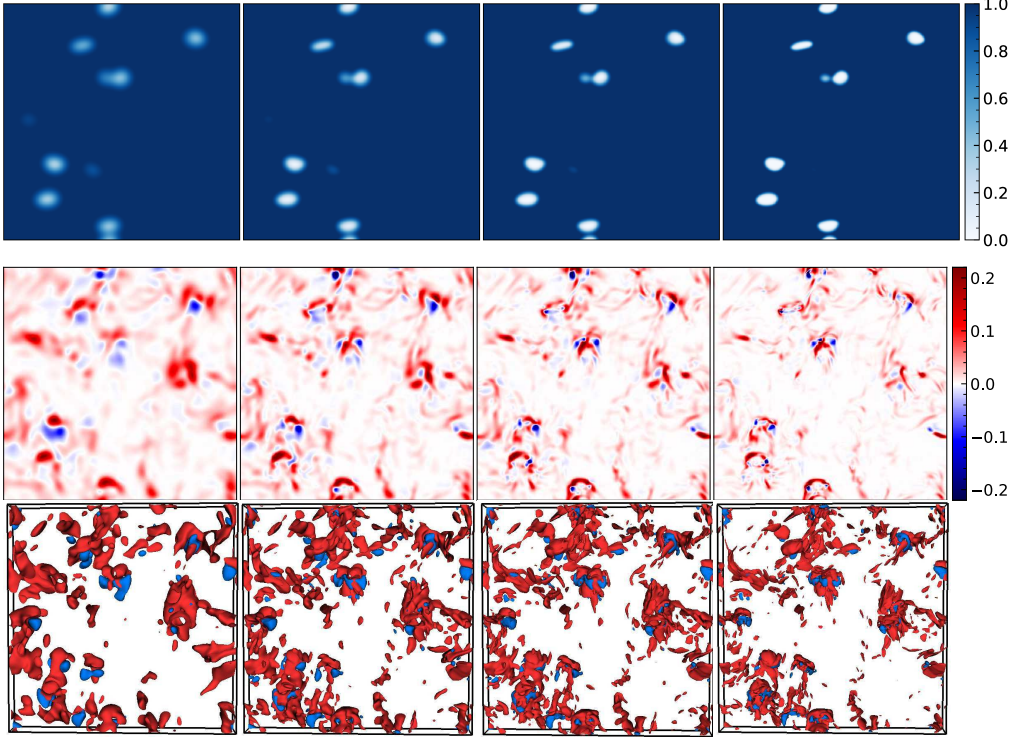


Figure 12: Buoyancy driven flow in presence of stirring ($b = 0.13, R3$). The pseudocolor plot of the filtered indicator function c (top panel) and the local nonlinear flux $\pi_K / \max(\pi_{k_d})$ (middle panel) in the $y = L/2$ plane. Constant- π_K isosurfaces for $|\pi_K| = 0.03 \max(\pi_{k_d})$ in a slab $L \times 2d \times L$ around the $y = L/2$ plane (bottom panel). The filter wavenumber (scale) is increased (decreased) from left to right $K/k_d = 0.6, 1.0, 1.4$ and 2.2 .

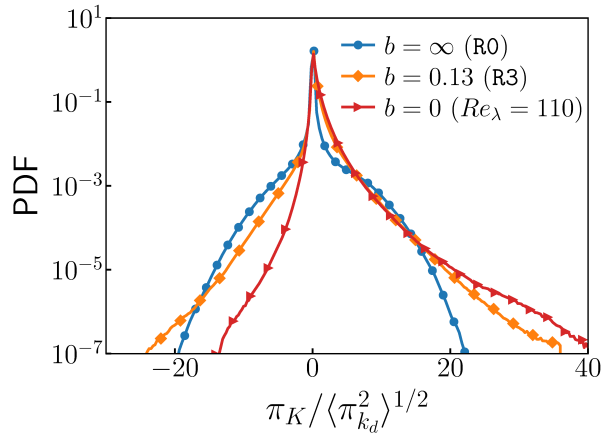


Figure 13: The PDF of the scaled nonlinear flux $\pi_K / \langle \pi_K^2 \rangle^{1/2}$ for different values of b , and with $K = k_d$.

3.7. Total energy budget

Using (2.1) we obtain the steady-state the total energy budget equation as

$$\varepsilon^g + \varepsilon^s = \varepsilon^\nu \quad (3.13)$$

i.e., energy injected by buoyancy and stirring is dissipated by viscosity. Using table 1, (3.13) is easily verified.

In this section, we study the contribution to the total budget from each of the phases. The two phases are characterized by the indicator function c which takes value 1 in the liquid phase, 0 inside the bubble and an intermediate value at the interface. In a DNS of two-phase flows, usually, the interface is diffused over to 3–4 grid points. Thus, using c to distinguish the phases implies that the interface region contributes to both the phases. In order to avoid this conundrum, we construct a new indicator function c' such that the interface points are included inside the bubble. To construct c' we first initialize it to be the same as c . The points which lie closest to $c' = 1/2$ contour are identified as bubble interface points. For points where $c' < 1/2$, c' is set to zero and it is unity outside. Next we set $c' = 0$ at all points that are within a distance of $0.16d$ from the interface points. This completes the procedure of generating an inflated region around each bubble.

Henceforth we shall use the term bubble to indicate the regions where $c' = 0$. Using c' we define the net injection and dissipation rates in the liquid as:

$$\varepsilon_1^\nu = 2\nu \langle c' \mathbf{S} : \mathbf{S} \rangle, \quad (3.14a)$$

$$\varepsilon_1^g = \langle c' \mathbf{u} \cdot \mathbf{F}^g \rangle, \quad (3.14b)$$

$$\varepsilon_1^s = \langle c' \mathbf{u} \cdot \mathbf{F}^s \rangle. \quad (3.14c)$$

The contribution from the bubble phase can be obtained by subtracting the contribution from the liquid phase from the total, for instance, dissipation rate in the bubble phase is $\varepsilon_b^\nu = \varepsilon^\nu - \varepsilon_1^\nu$.

In figure (14a,b) we show the pseudocolor plot of the local viscous dissipation $\varepsilon_{\text{loc}}^\nu(\mathbf{x}) = 2\nu \mathbf{S} : \mathbf{S}$. For the case with no stirring, $b = \infty$, the dissipation is strongly concentrated inside and in the wake of the bubbles, whereas when stirring is present, $b = 0.13$, strong dissipation is also observed in the liquid phase away from the bubbles.

In figure (15a) we look at the balance between energy injection and dissipation in each phase for the case of no stirring, $b = \infty$. In the liquid phase, viscous dissipation ε_1^ν far exceeds energy injected due to buoyancy ε_1^g , whereas in the bubble phase the situation is reversed. Note that the overall viscous dissipation inside the bubble phase is larger than the overall dissipation in the liquid phase.

We can now summarise the flow of energy completely for the case of no stirring, $b = \infty$. Buoyancy force injects energy at the scale of the bubbles, largely in the gas phase. A large fraction of this energy is dissipated within the bubble itself. Rest of it is transferred to the liquid phase by bubble-liquid interaction. Both the nonlinear flux and the flux due to the surface tension cascades this energy to smaller and smaller scales in the fluid. Energy dissipation happens in both the gas and liquid phase starting from the scale of bubble down to the smallest scales.

We next plot the injection and dissipation rates obtained for different phases for the case $b = 0.13$ in figure (15b). Here, we find that dominant energy injection is due to the stirring. This appears largely in the liquid phase. The net energy

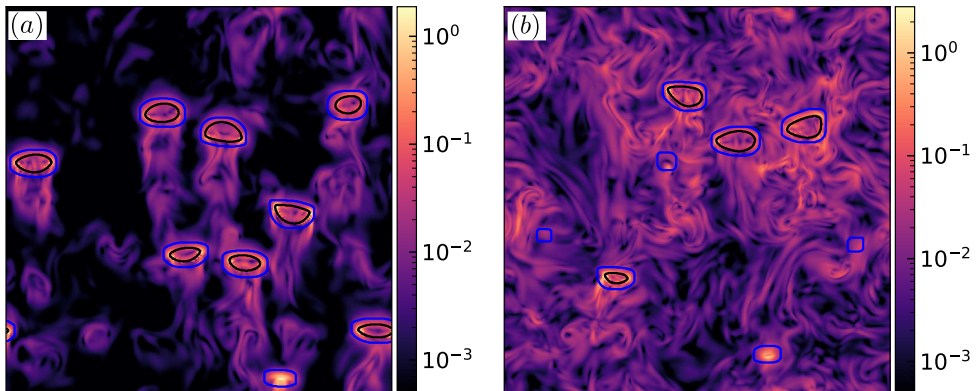


Figure 14: Pseudocolor plot of the local dissipation $\varepsilon'_{\text{loc}}$ in $y = L/2$ plane for (a) $b = \infty$ (run R0), and (b) $b = 0.13$ (run R3). The black line represents the bubble interface ($c = 0$ contour), and blue line indicates the contour $c' = 0$.

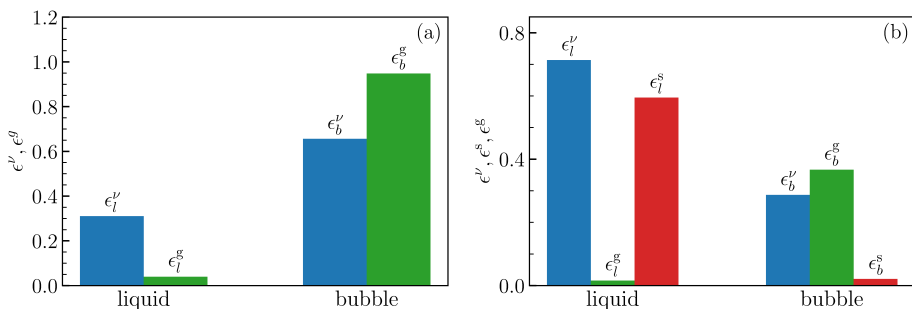


Figure 15: The dissipation and injection rates in the steady state evaluated in the liquid, and the bubble phase for (a) $b = \infty$ (run R0) and (b) $b = 0.13$ (run R3). The ordinate in both the figures is normalized by ε^ν

dissipated in the liquid phase exceeds the energy injected by stirring due to the additional energy transfer from the bubble phase to the liquid phase. In the bubble phase energy is injected by the buoyancy forces. Most of this energy is dissipated in the bubble phase, but as pointed out above, a part of it is also transferred to the liquid phase.

4. Conclusion

We conduct a DNS study of buoyancy-driven bubbly flow in the presence of large-scale stirring. We investigate the statistical properties of the flow and compare our findings with the experiments. Our key results are summarised below:

(i) The rise velocity of a bubble in the suspension reduces, and the liquid velocity fluctuations are rendered isotropic on increasing the stirring intensity.

(ii) Consistent with experiments (Lance & Bataille 1991; Prakash *et al.* 2016), we find the energy spectrum shows a Kolmogorov scaling for $k \ll k_d$ and a pseudo-turbulence scaling $-E(k) \sim k^{-3}$ – for $k \gg k_d$.

(iii) We rationalize the scaling observed in the energy spectrum by using a scale-by-scale energy budget analysis. For $k \ll k_d$, energy flux is the dominant

energy transfer mechanism although viscous dissipation is effective for all scales $k < k_d$. The balance of net production with viscous dissipation leads to the pseudo-turbulence scaling for $k \gg k_d$.

We want to emphasize that although we study turbulence modulation by weakly buoyant bubbles, the statistical properties of the flow are in qualitative agreement with the experiments (Lance & Bataille 1991; Prakash *et al.* 2016; Salibindla *et al.* 2020). Therefore, we believe that the energy transfer mechanisms discussed in our study should also apply to the experimental scenario of high density and viscosity contrast; our previous study (Pandey *et al.* 2020) already verified this in the absence of stirring.

However, we expect that the details of the wake structure in the vicinity of the bubble would depend on the density and viscosity contrast. How relevant is this for the energy transfer mechanism that we have proposed remains to be investigated. We hope that our results will motivate further investigations in this direction.

Appendix A. Boussinesq approximated Navier-Stokes equations

In this section we derive the Boussinesq approximate equations (2.1) starting from the following multiphase Navier-Stokes equations (Pandey *et al.* 2020):

$$\rho(c)D_t\mathbf{u} = \nabla \cdot (\mu(c)\mathbf{S}) + \mathbf{f}^\sigma + \mathbf{f}, \quad (\text{A } 1)$$

where the density field

$$\rho(c) = \rho_f c + \rho_b(1 - c), \quad (\text{A } 2)$$

the dynamic viscosity field $\mu(c) = \mu_f c + \mu_b(1 - c)$, $\rho_f(\mu_f)$ is the density (viscosity) of fluid phase, $\rho_b(\mu_b)$ is the density (viscosity) of the bubble phase, \mathbf{f}^σ is the surface tension force, $\overline{(\cdot)}$ the external force $\mathbf{f} \equiv [\rho(c)\mathbf{a} - \overline{\rho(c)\mathbf{a}}]$, \mathbf{a} is the acceleration, and in this section $\overline{(\cdot)}$ denotes spatial averaging. Note that as we work with periodic boundaries, our choice of external force ensures that no net momentum is added to the flow.

We assume small density contrast ($\text{At} \ll 1$) and identical dynamical viscosity of the two phases ($\mu_f/\mu_b = 1$). Thus we invoke Boussinesq approximation, whereby $\rho(c)$ on the left-hand side of (A 1) is replaced by the average density

$$\rho_a \equiv \overline{\rho(c)} = (\rho_f - \rho_b)c_a + \rho_b \approx (\rho_f + \rho_b)/2. \quad (\text{A } 3)$$

The above assumptions drastically simplify (A 1) to give,

$$D_t\mathbf{u} = \nu\nabla^2\mathbf{u} + \mathbf{F}^\sigma + \mathbf{F}, \quad (\text{A } 4)$$

where $\mathbf{F}^\sigma = \mathbf{f}^\sigma/\rho_a$ and $\mathbf{F} = \mathbf{f}/\rho_a$. The above equation is identical to the Boussinesq equation (2.1) that we use. Next we derive the buoyancy and the turbulent stirring force in the Boussinesq regime.

Using the definitions (A 2) and (A 3) in \mathbf{F} we get,

$$\mathbf{F} = \left[1 - \frac{(\rho_f - \rho_b)c_a}{\rho_a} \right] (\mathbf{a} - \overline{\mathbf{a}}) + \frac{(\rho_f - \rho_b)}{\rho_a} (c\mathbf{a} - \overline{c\mathbf{a}}). \quad (\text{A } 5)$$

When $\mathbf{a} = \mathbf{g}$, the first term on the right hand side of (A 5) is zero and we obtain

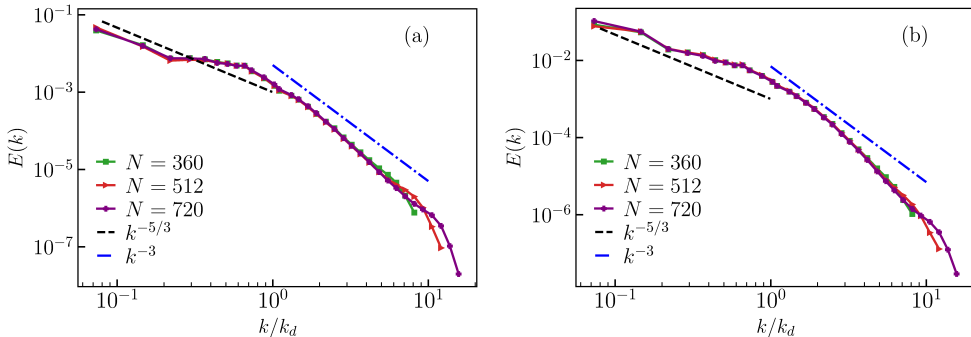


Figure 16: The kinetic energy spectra for R1 (left) and R3 (right) at resolutions $N = 360, 512$ and 720 .

the buoyancy force

$$\mathbf{F}^g = \frac{(\rho_f - \rho_b)}{\rho_a} (c - c_a) \mathbf{g} \approx 2At(c - c_a) \mathbf{g}. \quad (\text{A } 6)$$

On the other hand for turbulence stirring, we use an acceleration field with $\bar{\mathbf{a}} = 0$. Therefore, (A 5) simplifies to:

$$\mathbf{F}^s = \left[1 - \frac{(\rho_f - \rho_b)c_a}{\rho_a} \right] \mathbf{a} + \frac{(\rho_f - \rho_b)}{\rho_a} (ca - \bar{c}\mathbf{a}). \quad (\text{A } 7)$$

In the Boussinesq regime, $(\rho_f - \rho_b)/\rho_a \ll 1$ and we get $\mathbf{F}^s = \mathbf{a}$ to the leading order, i.e., the stirring force is applied irrespective of the phase or the indicator function. In the main manuscript we choose $\rho_a = 1$ everywhere.

Appendix B. Resolution test

To study grid convergence, we conduct DNS of turbulent bubbly flows for our runs R1 and R3 with increasing grid-resolution $N = 360, 512$, and 720 . The plot of the energy spectrum figure (16) clearly shows that even with $N = 360$, the inertial range as well as the k^{-3} scaling of pseudo-turbulence are well-captured. However, as expected, on increasing the grid-resolution the range of k^{-3} scaling obtained due the balance of net production with viscous dissipation extends. The departure from the k^{-3} scaling around $k \approx k_{\max}$ is an artifact of finite resolution.

Appendix C. Energy budget using sharp filter

We now present the result of the scale-by-scale energy budget analysis obtained by using a sharp low-pass filter instead of the Gaussian filter. The low-pass filtered velocity field for a sharp filter is defined as (Frisch 1997; Verma 2019; Pandey *et al.* 2020):

$$\mathbf{u}_K^<(x) = \sum_{q \leq K} \mathbf{u}_q \exp(iq \cdot x). \quad (\text{C } 1)$$

In figure (17a) we show the scale-by-scale budget obtained for the case $b = \infty$ and in figure (17b) we plot the budget for $b = 0.13$. By comparing with figure (8), it is clear that the choice of filtering does not qualitatively change the scale-by-scale energy budget. Our observations are consistent with the recent finding

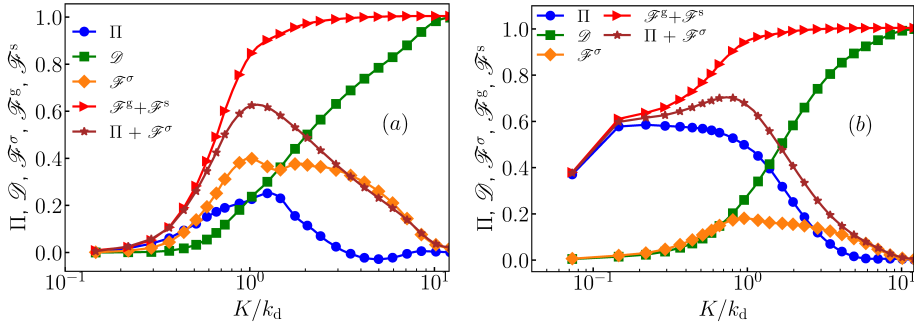


Figure 17: Scale-by-scale energy budget: plot of the energy flux Π_K , cumulative viscous dissipation \mathcal{D}_K , the surface tension contribution \mathcal{F}_K^σ , the cumulative energy injected due to buoyancy \mathcal{F}_K^g , and the energy injected due to turbulent forcing \mathcal{F}_K^s for (a) $b = \infty$, and (b) $b = 0.13$. In both the panels we normalize the ordinate by the viscous dissipation ε^ν .

of Alexakis & Chibbaro (2020) who did a similar comparison for homogeneous, isotropic turbulence.

Author contributions

V.P. performed the simulations. All authors contributed equally to analysing data and reaching conclusions, and in writing the paper.

Funding

This work was supported by the Department of Atomic Energy (DAE), India under Project Identification No. RTI 4007, DST (India) Project Nos. ECR/2018/001135 and DST/NSM/R&D_HPC_Applications/2021/29, and the Swedish Research Council Grant No. 638-2013-9243 as well as 2016-05225.

Declaration of interests

The authors report no conflict of interest.

REFERENCES

- ALEXAKIS, A. & CHIBBARO, S. 2020 Local energy flux of turbulent flows. *Phys. Rev. Fluids* **5**, 094604.
- ALMERAS, E., MATHAI, V., LOHSE, D. & SUN, C. 2017 Experimental investigation of the turbulence induced by a bubble swarm rising within incident turbulence. *J. Fluid Mech.* **825**, 1091–1112.
- ALMERAS, E., MATHAI, V., SUN, C. & LOHSE, D. 2019 Mixing induced by a bubble swarm rising through incident turbulence. *Int. J. Multiphase Flow* **114**, 316–322.
- ALMÉRAS, E., RISSO, F., ROIG, V., CAZIN, S., PLAIS, C. & AUGIER, F. 2015 Mixing by bubble-induced turbulence. *J. Fluid Mech.* **776**, 458–474.
- BALACHANDAR, S. & EATON, J.K. 2010 Turbulent dispersed multiphase flow. *Annu. Rev. Fluid Mech.* **42**, 111–133.
- BHATNAGAR, A., GUPTA, A., MITRA, D., PERLEKAR, P., WILKINSON, M. & PANDIT, R. 2016 Deviation-angle and trajectory statistics for inertial particles in turbulence. *Phys. Rev. E* **94**, 063112.

- BORUE, V. & ORSZAG, S.A. 1998 Local energy flux and subgrid-scale statistics in three-dimensional turbulence. *J. Fluid Mech.* **366**, 1–31.
- BUNNER, B. & TRYGGVASON, G. 2002a Dynamics of homogeneous bubbly flows part 1. rise velocity and microstructure of the bubbles. *J. Fluid Mech.* **466**, 17–52.
- BUNNER, B. & TRYGGVASON, G. 2002b Dynamics of homogeneous bubbly flows part 2. velocity fluctuations. *J. Fluid Mech.* **466**, 53 – 84.
- CANO-LOZANO, J.C., MARTÍNEZ-BAZÁN, C., MAGNAUDET, J. & TCHOUFAG, J. 2016 Paths and wakes of deformable nearly spheroidal rising bubbles close to the transition to path instability. *Phys. Rev. Fluids* **1**, 053604.
- CANUTO, C., HUSSAINI, M.Y., QUARTERONI, A.M. & ZANG, T.A. 2012 *Spectral Methods in Fluid Dynamics*. Springer-Verlag.
- CHANDRASEKHAR, S. 1981 *Hydrodynamic and Hydromagnetic Stability*. Dover Publications.
- CHEN, Q., CHEN, S., EYINK, G.L. & HOLM, D.D. 2003 Intermittency in the joint cascade of energy and helicity. *Phys. Rev. Lett.* **90**, 214503.
- CLIFT, R., GRACE, J.R. & WEBER, M. E. 1978 *Bubbles, drops and particles*. Academic Press.
- COX, S.M. & MATTHEWS, P.C. 2002 Exponential time differencing for stiff systems. *J. Comput. Phys.* **176**, 430–455.
- DECKWER, W.-D. 1992 *Bubbles Column reactors*. Wiley.
- EYINK, G.L. 1995 Local energy flux and the refined similarity hypothesis. *J. Stat. Phys.* **78**, 335–351.
- FRISCH, U. 1997 *Turbulence, A Legacy of A. N. Kolmogorov*. Cambridge University Press.
- HADAMARD, J. 1911 Mouvement permanent lent d’une sphere liquide et visqueuse dans un liquide visqueux. *C.R. Acad. Sci. Paris* **152**, 1735–1738.
- INNOCENTI, A., JACCOD, A., POPINET, S. & CHIBBARO, S. 2021 Direct numerical simulation of bubble-induced turbulence. *J. Fluid Mech.* **918**, A23.
- ISHIHARA, T., GOTOH, T. & KANEDA, Y. 2009 Study of high-reynolds number isotropic turbulence by direct numerical simulation. *Annu. Rev. Fluid Mech.* **41**, 165–180.
- KOLMOGOROV, A.N. 1941 The local structure of turbulence in incompressible viscous fluid for very large reynolds numbers. *Dokl. Acad. Nauk USSR* **30**, 9–14.
- KRAICHNAN, R.H. 1974 On kolmogorov’s inertial-range theories. *J. Fluid Mech.* **62**, 305–330.
- LANCE, M. & BATAILLE, J. 1991 Turbulence in the liquid phase of a uniform bubbly air–water flow. *J. Fluid Mech.* **222**, 95–118.
- LOISY, A. & NASO, A. 2017 Interaction between a large buoyant bubble and turbulence. *Phys. Rev. Fluids* **2**, 014606.
- MA, T., OTT, B., FRONHLICH, J. & BRAGG, A.D. 2021 Scale-dependent anisotropy, energy transfer and intermittency in bubble-laden turbulent flows. *arXiv:2104.00449* .
- MACHIELS, L. 1997 Predictability of small-scale motion in isotropic fluid turbulence. *Phys. Rev. Lett.* **79**, 3411–3414.
- MATHAI, V., LOHSE, D. & SUN, C. 2020 Bubbly and buoyant particle-laden turbulent flows. *Annu. Rev. Fluid Mech.* **11**, 529–559.
- MENEVEAU, C. & KATZ, J. 2000 Scale-invariance and turbulence models for large-eddy simulation. *Annu. Rev. Fluid Mech.* **32**, 1–32.
- MERCADO, J.M., GOMEZ, D.G., GILS, D.V., SUN, C. & LOHSE, D. 2010 On bubble clustering and energy spectra in pseudo-turbulence. *J. Fluid Mech.* **650**, 287–306.
- MUDDE, R. F. 2005 Gravity-driven bubbly flows. *Annu. Rev. Fluid Mech.* **37**, 393–423.
- PANDEY, V., RAMADUGU, R. & PERLEKAR, P. 2020 Liquid velocity fluctuations and energy spectra in three-dimensional buoyancy-driven bubbly flows. *J. Fluid Mech.* **884**, R6.
- PERLEKAR, PRASAD 2019 Kinetic energy spectra and flux in turbulent phase-separating symmetric binary-fluid mixtures. *Journal of Fluid Mechanics* **873**, 459–474.
- PETERSEN, M.R. & LIVESCU, D. 2010 Forcing for statistically stationary compressible isotropic turbulence. *Phys. Fluids* **22**, 116101.
- POPE, S. 2012 *Turbulent Flows*. Cambridge University Press.
- POPINET, S. 2018 Numerical models of surface tension. *Annu. Rev. Fluid Mech.* **50**, 1–28.
- PRAKASH, V. N., MERCADO, J.M., VAN WIJNGAARDEN, L., MANCILLA, E., TAGAWA, Y., LOHSE, D. & SUN, C. 2016 Energy spectra in turbulent bubbly flows. *J. Fluid Mech.* **791**, 174–190.

- RAMADUGU, R., PANDEY, V. & PERLEKAR, P. 2020 Pseudo-turbulence in two-dimensional buoyancy-driven bubbly flows: A dns study. *Eur. Phys. J. E* **43**, 73.
- RIBOUX, G., RISSO, F. & LEGENDRE, D. 2010 Experimental characterization of the agitation generated by bubbles rising at high reynolds number. *J. Fluid Mech.* **643**, 509–539.
- RISSO, F. 2011 Theoretical model for k^{-3} spectra in dispersed multiphase flows. *Phys. Fluids* **23**, 011701.
- RISSO, F. 2016 Physical interpretation of probability density functions of bubble-induced agitation. *J. Fluid Mech.* **809**, 240–263.
- RISSO, F. 2018 Agitation, mixing, and transfers induced by bubbles. *Annu. Rev. Fluid Mech.* **50**, 25–48.
- RISSO, F., ROIG, V., AMOURA, Z., RIBOUX, G. & BILLET, A.-M. 2008 Wake attenuation in large reynolds number dispersed two-phase flows. *Philos. Trans. R. Soc. A* **366** (1873), 2177–2190.
- ROGHAIR, I., ANNALAND, M. V. S. & KUIPERS, H. J. A. M. 2013 Drag force and clustering in bubble swarms. *AIChE Journal* **59** (5), 1791–1800.
- ROGHAIR, I., MERCADO, J. M., ANNALAND, M. V. S., KUIPERS, H., SUN, C. & LOHSE, D. 2011 Energy spectra and bubble velocity distributions in pseudo-turbulence: Numerical simulations vs. experiments. *Int. J. Multiph. Flow* **37**, 1093 – 1098.
- ROSTI, M.E. & BRANDT, L. 2018 Suspensions of deformable particles in a couette flow. *J. Non-Newton. Fluid* **262**, 3–11.
- ROSTI, M.E, BRANDT, L. & MITRA, D. 2018 Rheology of suspensions of viscoelastic spheres: deformability as an effective volume fraction. *Phys. Rev. Fluids* **3**, 012301.
- ROSTI, M. E., GE, Z., JAIN, S. S., DODD, M.S. & BRANDT, L. 2019 Droplets in homogeneous shear turbulence. *J. Fluid Mech.* **876**, 962–984.
- RYBCZYNSKI, D. 1911 Uber die fortschreitende bewegung einer flussigen kugel in einem zahen medium. *Bull. Acad. Sci. Cracovie* **1**, 40–46.
- SAID, E. 2019 Direct numerical simulation of turbulent flows laden with droplets or bubbles. *Annu. Rev. Fluid Mech.* **51**, 217–244.
- SALIBINDLA, A.K.R., MASUK, A.U.M., TAN, S. & NI, R. 2020 Lift and drag coefficients of deformable bubbles in intense turbulence determined from bubble rise velocity. *J. Fluid Mech.* **894**, A20.
- SHUKLA, I., KOFMAN, N., BALESTRA, G., ZHU, L. & GALLAIRE, F. 2019 Film thickness distribution in gravity-driven pancake-shaped droplets rising in a hele-shaw cell. *J. Fluid Mech.* **874**, 1021–1040.
- TABIB, M. V., ROY, S. A. & JOSHI, J. B. 2008 Cfd simulation of bubble column-an analysis of interphase forces and turbulence models. *Chem. Eng. J.* **139**, 589–614.
- TRYGGVASON, G., BUNNER, B., ESMAEELI, A., JURIC, D., AL-RAWAHI, N., TAUBER, W., HAN, J., NAS, S. & JAN, Y.-J. 2001 A front-tracking method for the computations of multiphase flow. *J. Comput. Phys.* **169**, 708 – 759.
- VERMA, M.K. 2019 *Energy transfers in fluid flows*. Cambridge University Press.
- YI, L., TOSCHI, F. & SUN, C. 2021 Global and local statistics in turbulent emulsions. *J. Fluid Mech.* **912**, A13.
- YOUSEFI, A., ARDEKANI, M.N. & BRANDT, L. 2020 Modulation of turbulence by finite-size particles in statistically steady-state homogeneous shear turbulence. *J. Fluid Mech.* **899**, A19.